ISSN 1995-0802, Lobachevskii Journal of Mathematics, 2022, Vol. 43, No. 7, pp. 1850–1865. © Pleiades Publishing, Ltd., 2022.

On the Convective Stability and Pattern Formation of Volumetrically Heated Flows with Asymmetric Boundaries

G. Cartland Glover[1*], S. C. Generalis[1], and E. C. Aifantis[2,3,4***]**

(Submitted by A. M. Elizarov)

[1] *Mathematics Department, College of Engineering and Physical Sciences, Aston University, Birmingham, B4 7ET United Kingdom*

[2] *School of Engineering, Aristotle University, Thessaloniki, 54124 Greece*

[3] *Michigan Technological University, Houghton, MI 49931 USA*

[4] *Friedrich-Alexander-University at Erlangen-Nurember, 90762 Fürth, Germany*

Received April 11, 2022; revised April 22, 2022; accepted April 30, 2022

Abstract—Non-linear solutions and their stability are presented for homogeneously heated fluids bounded by rigid conducting and insulating plates. In particular, we sought roll-type solutions emerging from the neutral stability curve for fluids with Prandtl numbers of 0.025, 0.25, 0.705, and 7. We determined the stability boundaries for the roll states in order to identify possible bifurcation points for the secondary flow in the form of regions that are equivalent to the Busse balloon. We also compared the stability exchange between "up" and "down" hexagons for a Prandtl number of 0.25 obtained from weakly non-linear analysis in relation to the fully non-linear analysis, consistent with earlier studies. Our numerical analysis showed that there are potential bistable regions for both hexagons and rolls, a result that requires further investigations with a fully non-linear analysis.

DOI: 10.1134/S1995080222100122

Keywords and phrases: *incompressible flow, bifurcation theory, homotopy method, stability, nonlinearity.*

1. INTRODUCTION

This work is concerned with convection and pattern formation generated by uniformly distributed internal heat sources in fluid layers that are bounded by rigid/insulating plates. It is motivated partially by previous work [1–6], as well as by the fact that the problem has many important environmental and industrial applications. Internally heated flows have received much less attention than Rayleigh-Bénard convection although they are directly related to studies of the earth's mantle, where heat sources can result from the decay of radioactive materials. Geophysical and planetary applications of volumetric heating also include the cases where heat is released by an electric current in a conductive fluid, or caused by internal heating associated with solar radiation in planetary atmospheres. Industrial applications of internally heated fluids include radioactive decay in molten reactor cores, as well as exothermic and endothermic reactions in chemical reactors.

In addition, the present problem can be compared with Rayleigh–Bénard convection, where fluid motions are driven by temperature differences across the fluid layer and not by homogeneous heating. The heating of horizontal internally heated fluid layers gives rise to stable convective structures [3, 7]. Typical structures observed in Rayleigh–Bénard convection [8] can take the form of two-dimensional rolls—Busse oscillations [9–12]. Three dimensional structures appear as hexagons, cross-rolls, bimodal cells and varicose type rolls [13–18]. In the case of internally heated convection in a horizontal layer with

*E-mail: greg_glover@email.com

**E-mail: s.c.generalis@aston.ac.uk

***E-mail: mom@mom.gen.auth.gr

asymmetric boundary conditions that is studied here, hexagonal and spoke-like structures have been observed experimentally at and beyond the transition between thermal conduction and convection [7, 19–21, 23].

Tveitereid and Palm (T&P) [24] examined pattern transitions from a laminar state of uniformly distributed internal heat sources in a fluid layer bounded by two plates; a rigid conducting plate above a rigid insulating plate where the two rigid boundaries are separated by a finite distance, with the azimuthal and its perpendicular directions of infinite extent.

They [24] employed a numerical method based on Fourier analysis combined with a modified Runge–Kutta method and found that hexagons can be stable for values up to 15 times the critical Rayleigh number at infinite Prandtl number. The temperature equation decouples from the momentum equation rendering the problem much simpler to deal with, when the Prandtl number is infinite. Weakly nonlinear analysis was also applied with the Boussinesq approximation [24], which found that the only stable planform for small supercritical Rayleigh numbers are the hexagons. The weakly nonlinear results were derived on the basis of the cubic order approximation and, therefore, this analysis is only valid for heating close to the critical Rayleigh number.

T&P [24] further confirmed the existence of a small subcritical regime and found that at Prandtl numbers less than 0.25, the stable planform takes the form of "up-hexagons". Thess and Bestehorn [26] also reported a similar exchange between hexagon types in Bénard Marangoni convection, where up-hexagons occur at Prandtl numbers greater than the critical value. Both studies report rolls as the dominant planforms at such transition of Prandtl number [24, 26].

It should be noted here that T&P used a small number of modes in their simulations, compared to today's hardware capabilities, and while their simulations were initialised by different states, they always "resolved" to down hexagons. Their stability analysis concurs this statement ([24, Fig. 1]), where they quote that all their solutions, and with increasing time, approach a hexagon pattern with downward motion at the centre of each shell. Comparisons made against experimental [23, 27] and theoretical studies [25, 28], though [24] support the above results and are also supported by recent experimental studies [20–22, 29], as well as recently reported direct numerical simulations [30], where a non-zero heat flux was applied to the lower boundary. However, rolls were found to be unstable at high Prandtl numbers and for wavenumbers much larger than the critical wavenumber associated in experiments under such internal heating conditions [7].

Therefore, the principal aim of this paper is to explore the linear stability of hexagons and rolls from the region of the critical transition bifurcation number to approximately 10 times this value. This is motivated by the desire to offer a complete stability boundary for each of the primary states that bifurcate from the neutral curve. We have examined the stability characteristics of such roll and hexagon patterned solutions for a variety of Prandtl numbers and against different types of perturbations. In this sense our work complements and enhances the work of T&P [24], which was either limited to weakly non-linear analysis or employed the large Prandtl number value limit. In addition, we also offer an appendix, where the effect of the Prandtl number on the stability of hexagons is evaluated via explicit calculations for a variety of Prandtl number values, where we also established regions of stable rolls that could be related to the exchange of stability between the "up" and "down" hexagon states. We also applied disturbances to the rolls in order to establish an equivalent to Busse's [9] balloon under the assumed conditions (i.e., internal heating with conducting/insulating boundaries for Prandtl numbers up to 7). This allowed us to examine the limits of stability of the rolls and hexagons at several Prandtl numbers and compare results against the T&P [24] results. We also show numerically that our simulations are in complete agreement with the recent work of Busse [10].

In Section 2, we present the formulation for our problem along with the corresponding geometric configuration. In Section 3, we present the stability analysis of fully non-linear steady hexagon and roll solutions for the Prandtl numbers of several fluids. Our conclusions are summarised in Section 4, while the appendix contains supplementary material.

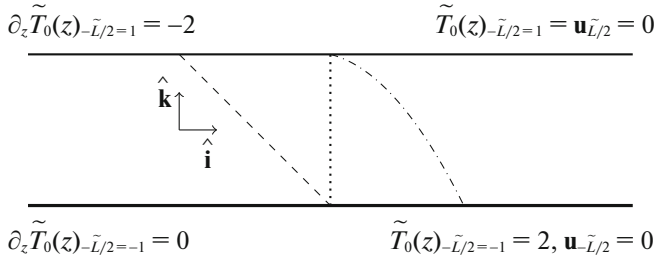

Fig. 1. Two-dimensional view of the geometrical configuration with the boundary conditions that are applied to a horizontal fluid layer between a conducting and an insulating boundaries. The dash-dotted curve $(T_0(z)/Gr = -(z^2 + 2z - 3)/2)$ and the dashed line $(\partial_z T_0(z)/Gr = -(1 + z))$ indicate the basic (laminar) temperature profile and its derivative over the layer depth. The dotted line indicates the basic (laminar) velocity profile. $\hat{\mathbf{i}}$, $\hat{\mathbf{j}}$, $\hat{\mathbf{k}}$ are the unit Cartesian vectors ($\hat{\mathbf{j}}$ is perpendicular to the $\hat{\mathbf{i}}$, $\hat{\mathbf{k}}$ plane and is not depicted).

2. FORMULATION

In this study, we assume quiescent incompressible Newtonian fluids with thermal diffusivity $\tilde{\kappa}$ and kinematic viscosity $\tilde{\nu}$ confined between two parallel horizontal plates of infinite extent. The coordinate system (x, y, z) comprises both horizontal and the normal the the wall directions, respectively, with the origin positioned on the midplane of the layer. The plates are a distance $\tilde{L}$ apart with the upper plate is maintained at the reference temperature $\tilde{T}_{\tilde{L/2}} = \tilde{T}_r$, while the lower plate is an insulating surface with $\partial_{\tilde{z}} \tilde{T}_{-\tilde{L/2}} = 0$, as is also shown in Fig. 1.

2.1. Governing Equations

The motion of the fluid is driven by its response to the internal heating, which gives rise to local differences in the density due to thermal expansion. The local variations in the density are assumed to be small enough for the Boussinesq approximation to be valid [8, 31, 32]. The fluid motion can be modeled by the following governing equations for the velocity $\tilde{\mathbf{u}}$ and the temperature deviation $\tilde{T}$ from the environment $\tilde{T}_r$:

$$\tilde{\boldsymbol{\nabla}} \cdot \tilde{\mathbf{u}} = 0, \tag{1}$$

$$\tilde{\rho}\left(\partial_{\tilde{t}} \tilde{\mathbf{u}} + (\tilde{\mathbf{u}} \cdot \tilde{\boldsymbol{\nabla}})\tilde{\mathbf{u}}\right) = -\tilde{\boldsymbol{\nabla}}\tilde{p} + \tilde{\mu}\tilde{\nabla}^2 \tilde{\mathbf{u}} - \tilde{\beta}\tilde{\rho}\tilde{\mathbf{g}}\left(\tilde{T} - \tilde{T}_r\right), \tag{2}$$

$$\partial_{\tilde{t}} \tilde{T} + (\tilde{\mathbf{u}} \cdot \tilde{\boldsymbol{\nabla}})\tilde{T} = \tilde{\kappa}\tilde{\nabla}^2 \tilde{T} + \tilde{q}, \tag{3}$$

where $\tilde{(\cdot)}$ indicates a dimensional variable, with $\tilde{q}$ being the rate of internal heating supplied to the layer. The parameters $\tilde{\beta}$, $\tilde{\mu}$, and $\tilde{\rho}$ are the thermal expansion coefficient, the dynamic viscosity and the density at the reference temperature $\tilde{T}_r$. The kinematic viscosity is given by $\tilde{\nu} = \tilde{\mu}/\tilde{\rho}$, while $\tilde{\mathbf{g}}$ is the uniform gravitational acceleration with $g = |\tilde{\mathbf{g}}|$.

In order to non-dimensionalise Eqs. (1)–(3) we use L, $L^2/\tilde{\nu}$, and $qL^2/(2\tilde{\kappa}Gr)$ as the dimensions of the system with respect to length, time and temperature. The Grashof number Gr is a control parameter for the ratio of buoyancy driven flow to inertially driven flow and it indicates the heat required for the fluid state in the layer to be in the convection region. It is defined as $Gr = \left(\tilde{g}\tilde{\beta}\tilde{q}\tilde{L}^5\right)/\left(2\tilde{\nu}^2\tilde{\kappa}\right)$ and is used to study convection beyond the critical (basic, laminar) state by also assuming no-slip boundary conditions for the velocity deviations from the basic fluid state. The Prandtl number, Pr is defined by $Pr = \tilde{\nu}/\tilde{\kappa}$ and the corresponding Rayleigh number by $Ra = Pr\ Gr$. The dimensionless velocity $\tilde{\mathbf{u}}$ and temperature $\tilde{T}$ deviations from the pure conduction state, are then governed by

$$\boldsymbol{\nabla} \cdot \mathbf{u} = 0, \tag{4}$$

$$\partial_t \mathbf{u} + (\mathbf{u} \cdot \boldsymbol{\nabla})\mathbf{u} = -\boldsymbol{\nabla} p + \nabla^2 \mathbf{u} - \frac{\mathbf{g}}{g} T, \tag{5}$$

$$\partial_t T + (\mathbf{u}\cdot\boldsymbol{\nabla})T = \frac{1}{Pr}\left(\nabla^2 T + 2Gr\right). \tag{6}$$

In order to obtain the basic (purely conductive, laminar) temperature profile, we ignore the velocity and temperature deviations perturbations in Eqs. (5), (6) and solve the resulting ordinary differential equations subject to the boundary conditions of Fig. 1. This gives $T_r(z) = -Gr \times (z^2 + 2z - 3)/2$, $\mathbf{u}_r(z) = 0$, for the basic temperature and velocity profiles of Fig. 1. More details of the generic methodology can be found in [2, 3, 33] and more recently in [34].

Following [24, 28], the critical Rayleigh number for the transition between laminar conduction and steady convection is taken as $Ra_c = 2772.27$. The wavenumber of the state observed at critical transition is $\alpha_c = 2.63$. We have confirmed the form of neutral stability boundary and the critical values in [6]. In this work we concentrate on the stability of non-linear roll and hexagon solutions, selecting the values of $Pr = 0.025, 0.25, 0.705, 7$ for our numerical analysis. Since regular wave-like motion is expected with the formation of primary rolls or hexagons, the steady flow and temperature are expanded in the x, y plane by N_x and N_y modes using a double Fourier series. In the z direction, we apply N_z modes of a Chebyshev expansion for the steady flow, while for temperature we employ N_z modes of a Chebyshev polynomial expansion defined in terms of a gradient in order to take into account the asymmetric boundary conditions. Thus we have

$$u_j(x,y,z) = \sum_{n_x=-N_x}^{N_x}\sum_{n_y=-N_y}^{N_y}\sum_{n_z=0}^{N_z} \hat{u}_j(n_x,n_y,n_z)(1-z^2)^{J(j)}T_{n_z}(z)e^{\imath n_x\alpha_x x}e^{\imath n_y\alpha_y y}, \tag{7}$$

$$\theta(x,y,z) = \sum_{n_x=-N_x}^{N_x}\sum_{n_y=-N_y}^{N_y}\sum_{n_z=0}^{N_z} \hat{\theta}(n_x,n_y,n_z)U_{n_z}(z)e^{\imath n_x\alpha_x x}e^{\imath n_y\alpha_y y}, \tag{8}$$

where $T_{n_z}(z)$ is the n_z order Chebyshev polynomial and $U_{n_z}(z)$ is the n_z order shifted Chebyshev polynomial, given by

$$U_{n_z}(z) = T_{n_z}(z) + \frac{\left[n_z^2 - (n_z-2)^2\right]\, T_{n_z-1}(z) - \left[n_z^2 + (n_z-1)^2\right]\, T_{n_z-2}(z)}{(n_z-1)^2 + (n_z-2)^2}. \tag{9}$$

Both $\hat{u}_j(n_x,n_y,n_z)$ and $\hat{\theta}(n_x,n_y,n_z)$ are complex coefficients for the velocity and temperature deviations taking into account the boundary conditions for the temperature (see Fig. 1). The function $J(j)$ takes the value 1 for $j \in \{x,y\}$ and 2 for $j = z$. The non-slip boundary condition for the velocity $\mathbf{u}$ is automatically satisfied by the factor $(1-z^2)^{J(j)}$ and its derivative. Taking into account the imposed horizontal translation and wall-normal reflectional symmetries, as well as the continuity equation, a Galerkin-type projection yields quadratic equations for the truncated independent set of coefficients of the series. The Newton–Raphson method enables us to determine the solutions of the equations for the rolls and hexagons, to a high degree of accuracy [2, 34].

2.2. Truncation

Here we present the dependence of the complex coefficients, mean temperature and its gradient on the truncation level (see Tables 1 and 2). For the complex coefficients, we just depict the numerical values of the real part of $\hat{u}_z(0,1)$ for rolls and of $\hat{u}_z(0,1,0)$ for hexagons at various truncation levels, as well as, the strength of the secondary flow, expressed by ℓ^2_{norm} (Tables 1 and 2). We also show the convergence in the mean convective temperature at the lower insulating boundary and the gradient of the mean convective temperature at the upper conducting boundary. In order to ensure high accuracy of our stability results, we chose $N_x = 5, N_y = 0, N_z = 13$ for the rolls (Table 2) and $N_x = 10, N_y = 6, N_z = 9$ for both types of hexagon (Table 1) at $Pr = 0.025$ and $Ra = 1.01Ra_c$. These values were retained for the analysis of the rolls for all Prandtl numbers considered here.

Table 1. Truncation level dependence of the roll solutions from our simulations at $\alpha_x = 1.315$ for $Pr = 0.025$ at $Ra = 1.01Ra_c$, where the subscript c indicates critical value(s). Here we present the dependence of the truncation on the real part of $\hat{u}_z(0,1)$ and the $\ell^2_{\text{norm}} = \sqrt{\sum_{n_x=-N_x}^{N_x} \sum_{n_z=0}^{N_z} \hat{u}_j(n_x,n_z) \times \hat{u}_j(n_x,n_y,n_z)^*}$, which is a measure of the strength of the convective flow. The complex conjugate is denoted by $*$, while the superscript R denotes the real part. The mean temperature of the fluid and its derivative are given by $\langle T(z)\rangle = \sum_{n_z=0}^{N_z} \hat{\theta}(n_z) U_{n_z}(z)$, $\partial_z\langle T(z)\rangle = \sum_{n_z=0}^{N_z} \hat{\theta}(n_z)\partial_z U_{n_z}(z)$ respectively, with the boundary conditions for the basic temperature and its derivative given by $T_0(-1) = 2.00$ and $\partial_z T_0(1) = -2.00$ respectively (see also Fig. 1). The derivative of the mean temperature is calculated using Eq. (9) and we provide a sample of values of the mean temperature and its derivative

N_x	N_y	N_z	$\hat{u}_z^R(0,1,0)$	ℓ^2_{norm}	$\langle T(-1)\rangle$	$\partial_z\langle T(1)\rangle$
10	6	5	−0.00146237	0.66589599	−0.00059418	0.00001043
10	6	7	−0.00147608	0.67277968	−0.00058739	−0.00000163
10[a]	6	9	-0.00146736	0.67180251	−0.00058705	0.00000014
10	6	11	−0.00146726	0.67176162	−0.00058699	0.00000000
10	6	13	−0.00146740	0.67177616	−0.00058699	0.00000000
10	6	15	−0.00146739	0.67177544	−0.00058700	0.00000000
4	4	15	−0.00142418	0.67027414	−0.00058463	0.00000000
6	4	15	−0.00146679	0.67174780	−0.00058696	0.00000000
6	6	15	−0.00146676	0.67174794	−0.00058696	0.00000000
8	6	15	−0.00146740	0.67177547	−0.00058700	0.00000000
8	8	15	−0.00146740	0.67177547	−0.00058700	0.00000000
10	8	15	−0.00146739	0.67177544	−0.00058700	0.00000000
10	10	15	−0.00146739	0.67177544	−0.00058700	0.00000000

[a] This truncation level was maintained for both the strongly nonlinear states and their stability analysis against perturbations.

2.3. Stability

To find the secondary states that evolve from the primary rolls and the hexagons, we determine the growth rate σ of infinitesimal disturbances. The growth rates are calculated by using the traditional linear stability theory based on modal analysis:

$$\delta u_j(x,y,z,t) = e^{\sigma t} \sum_{n_x,n_y,n_z} \delta\hat{u}_j(n_x,n_y,n_z)(1-z^2)^{J(j)} T_{n_z}(z) e^{in_x(\alpha_x+d)x} e^{in_y(\alpha_y+b)y}, \tag{10}$$

$$\delta\theta(x,y,z,t) = e^{\sigma t} \sum_{n_x,n_y,n_z} \delta\hat{\theta}(n_x,n_y,n_z) U_{n_z}(z) e^{in_x(\alpha_x+d)x} e^{in_y(\alpha_y+b)y}, \tag{11}$$

where (d,b) are the Floquet multipliers, representing here the wavenumbers of the imposed disturbances on the flow states at hand. The Fourier series when substituted in the equations of motion of the fluid flow leads to a generalized eigenvalue problem [2]. We solve this eigenvalue problem and we designate a state as stable if for all real parts $\text{Re}[\sigma] < 0$ and, accordingly, unstable if for any real part $\text{Re}[\sigma] > 0$, where σ represents a complex eigenvalue of the generalised eigenvalue problem for the disturbances. We seek the maximum value of the real part (growth rate) of the eigenvalues to determine disturbances that cause the secondary states to evolve from the primary rolls. Several values of Ra were studied and the maximum real part of the most critical eigenvalue (the one that initiates the transition of the flow to its secondary state) was evaluated. It is worth mentioning here that in all cases examined, the symmetry relations $\text{Re}[\sigma(d,b)] = \text{Re}[\sigma(\pm d,b)]$ (b fixed), $\text{Re}[\sigma(d,b)] = \text{Re}[(\sigma)(d,\pm b)]$ (d fixed) and $\text{Re}[\sigma(d,b)] = \text{Re}[\sigma(\pm d,b)]$, were always observed, despite of the fact that the finite truncation levels

Table 2. Truncation level dependence of the hexagon solutions at $\alpha_x = 0.6575$ and $\alpha_y = 1.1388$ for $Pr = 0.025$ at $Ra = 1.01Ra_c$. Here we present the dependence of the truncation on the real part of $\hat{u}_z^R(0,1,0)$ and the value of $\ell^2_{\text{norm}} = \sqrt{\sum_{n_x=-N_x}^{N_x}\sum_{n_y=-N_y}^{N_y}\sum_{n_z=0}^{N_z}\hat{u}_j(n_x,n_y,n_z)\times\hat{u}_j(n_x,n_y,n_z)^*}$, see Table 1, where $*$ denotes complex conjugate, while the superscript R designates the real part. The mean temperature and its derivative is defined as in Table 1

N_x	N_z	$\hat{u}_1^R(0,1,0)$	ℓ^2_{norm}	$\langle T(-1)\rangle$	$\partial_z\langle T(1)\rangle$
5	3	1.56308958	1.56741561	−0.00192686	0.00006023
5	5	1.28723257	1.29070183	−0.00148694	0.00001844
5	7	1.34214006	1.34589050	−0.00157063	−0.00000260
5	9	1.34086062	1.34460363	−0.00157139	0.00000022
5	11	1.34085653	1.34459959	−0.00157121	0.00000000
2	13	1.30731404	1.31102563	−0.00149331	0.00000000
4	13	1.34086190	1.34460500	−0.00157122	0.00000000
5[a]	13	1.34085732	1.34460038	−0.00157121	0.00000000
6	13	1.34085732	1.34460038	−0.00157121	0.00000000
5	15	1.34085728	1.34460035	−0.00157121	0.00000000

[a] This truncation level was maintained for both the strongly nonlinear states and their stability analysis against perturbations.

given in Tables 1–2 were used. We varied (d, b) in steps of 0.1 between 0 and $2.3\alpha_c$ when either d or b were fixed. When both d and b were varied, we only examined (d, b) up to $0.7\alpha_c$.

3. RESULTS OF STABILITY CALCULATIONS

In this section, we provide stability results for primary rolls for fluids in an internally heated fluid layer with $Pr = 0.025, 0.25, 0.705, 7.0$, as well as for hexagonal states at $Pr = 0.025, 0.705, 0.8$.

3.1. Rolls at $Pr = 7$

In Fig. 2, we present the results of our numerical analysis for the case $Pr = 7$. The stable region is confined by the outer linear neutral curve (L), the cross-roll (CR), the Eckhaus (E), the knot (K), the skewed-varicose (SV), and the zig-zag (ZZ) instability boundaries [15, 16, 18]. The relevant values of (d, b) are clearly indicated in Fig. 2. These boundary curves were evaluated for a range of the Floquet parameters (d, b) as indicated in Fig. 2.

The boundaries of the Eckhaus curves are presented, where the maximum growth rate was observed over a number of values of the Floquet parameter d, keeping $b = 0$ [16, 18, 34]. The Eckhaus curve bounds the area of the stable waves towards larger (1.36 and 1.46) and lower (1.18 and 1.26) wavenumbers at $1.01Ra_c$. We use a similar analysis to obtain the maximum growth rates for the cross-roll and knot instabilities by varying b and keeping $d = 0$ [18]. In this case we select $\alpha = 1.1$ and plot a number of values of Ra between Ra_c and $4.04Ra_c$ to find peak values in the growth rates. This gave two peaks, one for the cross-roll instability for $b \approx \alpha_c$ and the other for the knot instability for $b \ll \alpha_c$, as indicated in Fig. 2. The zig-zag instability is also found by varying b and keeping $d = 0$, but in this case we chose the first instability to cross the linear boundary at small values of b. The limits and values of skewed varicose instabilities were found by varying both b and d, while keeping $Ra = 2.02Ra_c$ and $\alpha = 1.335$ fixed [18]. We selected the disturbances, which gave the maximum growth rate and where $b/d \approx 1$. As hexagons are known to be the preferred state at the bifurcation point from the laminar state [24], we subsequently tested the stability of the rolls against the hexagonal disturbances. Both combinations of $(\alpha_c/2, \sqrt{3}\alpha_c/2)$ were applied to (d, b). The hexagonal instability with $(d, b) = (\sqrt{3}\alpha_c/2, \alpha_c/2)$indicates that the rolls are stable once $Ra \geq 1.25Ra_c$, thus suggesting

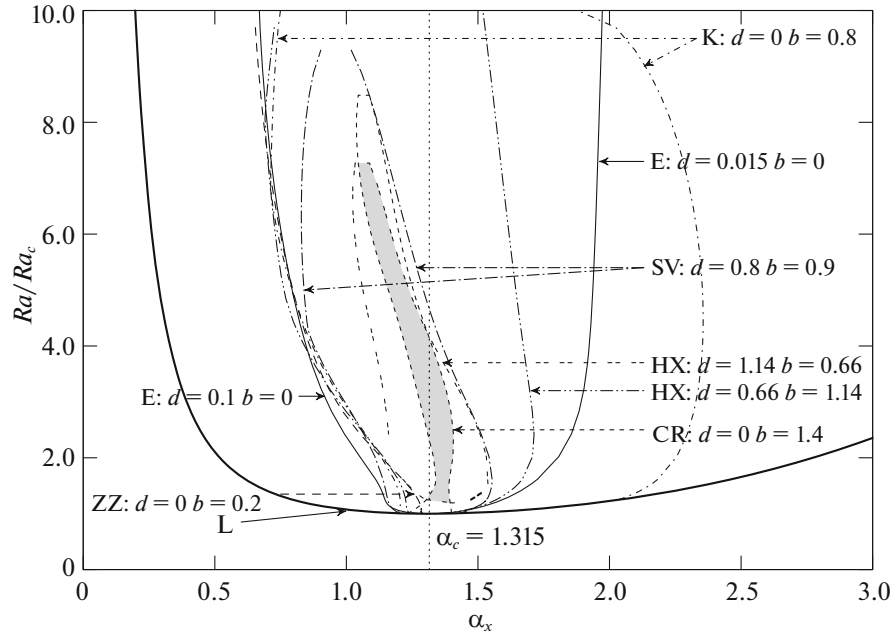

Fig. 2. Stability plots for rolls at $Pr = 7$. The shaded region indicates where stable rolls exist. Thin black curves indicate stability limits of the rolls with respect to arbitrary three dimensional perturbations. Thick black lines indicate oscillating instabilities (except for the linear neutral, L, curve).

that the region inside the cross-roll instability loop is where stable rolls are expected to occur. In the case of the hexagonal instability with $(d, b) = (\sqrt{3}\alpha_c/2, \alpha_c/2)$, oscillating instabilities occur, where a significant pair of conjugate complex eigenvalues emerge.

3.2. Rolls at $Pr = 0.705$

In Fig. 3, the stability diagram is illustrated for the case of $Pr = 0.705$. The stable region is enclosed by the linear neutral curve, the cross-roll, the Eckhaus, the knot, the skewed-varicose and the zig-zag instability boundaries. In addition to these instabilities, we also present the stability boundaries for the oscillatory (O) and oscillatory skewed varicose (OSV) instabilities [17]. The relevant values of (d, b) are clearly indicated in the figure.

For $Pr = 7$, the cross-roll and knot instability boundaries were selected from the growth rate maxima as b was varied. We identified the boundary for the oscillatory instability by varying b with $d = 0$ and determined the maximum growth rate of the disturbances complex conjugates eigenvalues [16, 18]. We found the boundaries of the skewed varicose instability for $Pr = 0.705$ in the same way as for $Pr = 7$ by varying both b and d, by also adjusting to $Ra = 2.85Ra_c$ and $\alpha = 1.335$ for the (d, b) indicated in Fig. 3 [18]. At this value of Ra, we found that a conjugate pair of complex eigenvalues occur, suggesting the emergence of oscillatory skewed varicose instabilities. Such instabilities occur in a small region on the skewed varicose boundary in Fig. 3 at about $3Ra_c$. A second boundary of oscillatory skewed varicose instabilities with the same (d, b) was observed above the boundary for such oscillatory instabilities. Applying both combinations of the hexagonal type instabilities $(d, b) = (\alpha_c/2, \sqrt{3}\alpha_c/2)$, we found two loops encircling the stable roll region bounded by the zig-zag, skewed varicose and oscillatory instabilities. As for the case of $Pr = 7$, the hexagonal instability with $(d, b) = (\sqrt{3}\alpha_c/2, \alpha_c/2)$ suggests that the rolls are stable when Ra is greater than Ra_c (at $Pr = 0.705$, $Ra = 1.17Ra_c$). The size of the stable region increases between $0.705 < Pr < 7.0$ in a manner that is consistent with [9, 15, 16]. Oscillating instabilities were found, where we observed a conjugate pair of complex eigenvalues for both hexagonal instabilities, particularly in the region above $(d, b) = (0, 1.1)$.

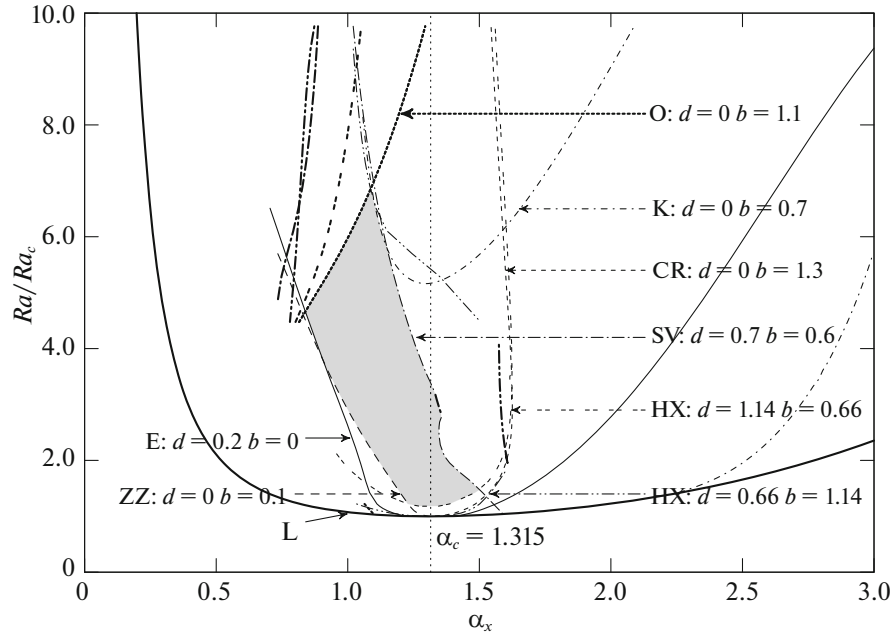

Fig. 3. Stability plots for rolls at $Pr = 0.705$. The shaded region and the various stability boundary curves shown here have the same meaning as in Fig. 2.

3.3. Rolls at $Pr = 0.025$

For the case of $Pr = 0.025$, the stability boundaries of the two dimensional roll structures are shown in Fig. 4. They consist of the Eckhaus, hexagonal, oscillatory and skewed-varicose instability boundaries surrounding a small stable region just beyond the linear neutral curve.The change in the size of the small stable region as Pr decreasing is again consistent with earlier studies reported in [9, 15, 16]. Note that the hexagonal instability with $(d, b) = (\sqrt{3}\alpha_c/2, \alpha_c/2)$ limits the region of stable rolls in the same way as $Pr = 0.705, 7$. The relevant values of (d, b) are clearly indicated in Fig. 4.

3.4. Rolls at $Pr = 0.25$

Figure 5 illustrates the stability diagram in the case of $Pr = 0.25$. We selected a Prandtl number value of 0.25 to analyse the stability of the "up" and "down" hexagons, as well as the primary rolls, in order to determine whether such instabilities exchange between the "up" and "down" hexagon that was reported by Tveitereid and Palm is observed by using our fully non-linear code [24]. We observe a small stable region just beyond the linear neutral curve that is surrounded by Eckhaus, oscillatory, as well as both types of hexagonal stability boundaries.The extent to which rolls remain stable is significantly shorter than for fluids at $Pr = 0.705, 7$, yet longer than those at $Pr = 0.025$. The relevant values of (d, b) are clearly indicated in Fig. 5.

3.5. Hexagonal States

The limits of stability of the rolls, "up" and "down" hexagons in terms of Ra were established via weakly non-linear analysis [24] as quadratic functions (P_n) of Pr, which have the form

$$P_0 = -14.71 + 3.687Pr^{-1}, P_1 = 8.639 - 0.0284Pr^{-1} + 0.0373Pr^{-2},$$

$$P_2 = 10.40 + 0.4707Pr^{-1} + 0.2088Pr^{-2}, P_3 = P_2 - P_1, P_4 = 0.25(P_1 + P_2), P_5 = 2P_2 + P_1,$$

$$Ra(Pr)_{\min(HX)} = -P_0^2/4P_5, Ra(Pr)_{\min(HX,RL)} = P_0^2P_1/P_3^2, Ra(Pr)_{\min(RL)} = P_0^2(P_1 + 4P_4)/P_3^2.$$

$Ra(Pr)_{\min(HX)}$ indicates the Ra value of the turning point in the subcritical branch of the hexagons, whereas $Ra(Pr)_{\min(HX+RL)}$ is the minimum limit for bistability of hexagons and rolls, whereas $Ra(Pr)_{\min(RL)}$ is the minimum limit of stability for just rolls.

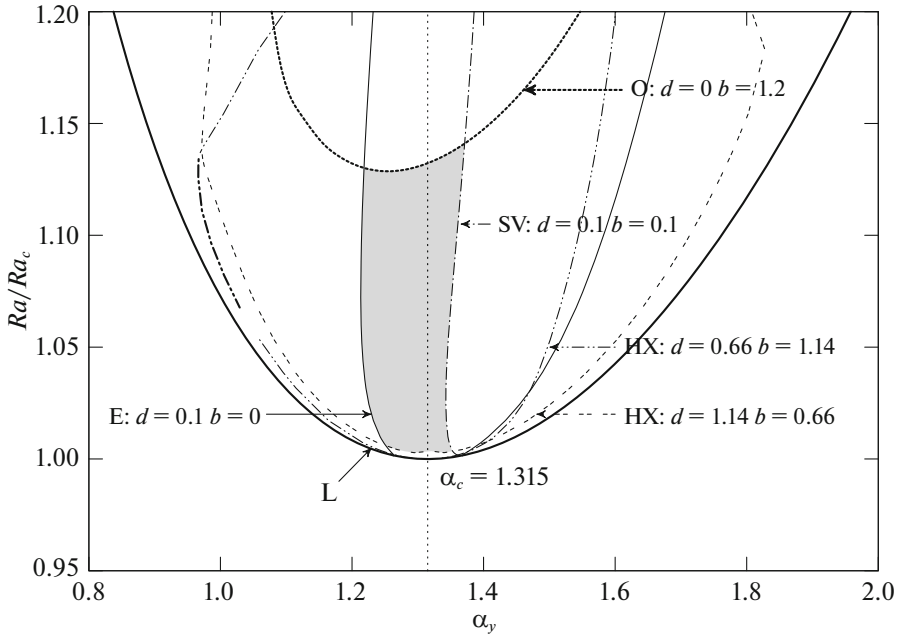

Fig. 4. Stability plots for rolls at $Pr = 0.025$. The shaded region and the various types of stability curves shown have the same meaning as in Fig. 2.

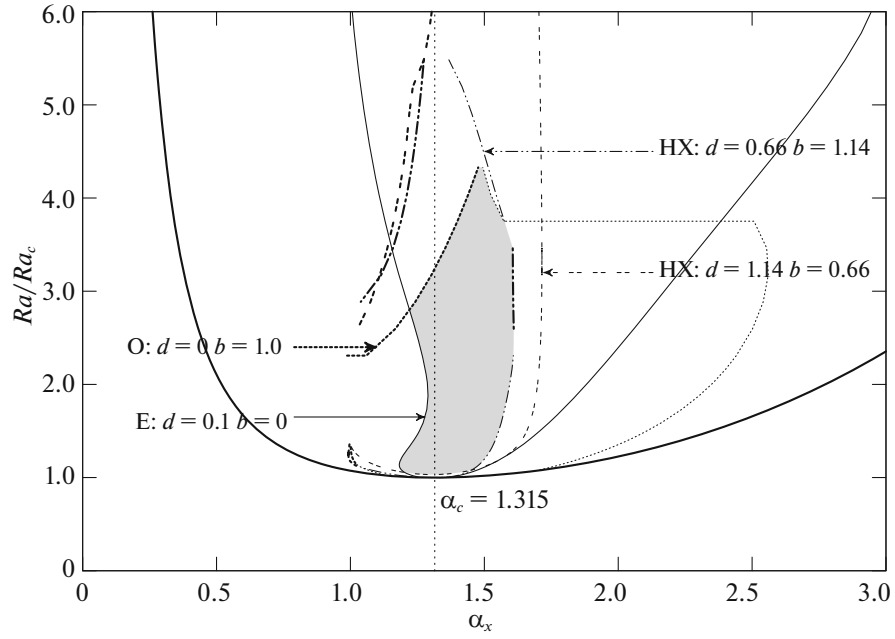

Fig. 5. Stability plots for rolls at $Pr = 0.25$. The shaded region and the various types of stability curves shown have the same meaning as in Fig. 2.

In Fig. 6 we plot the stability curves for rolls and hexagons for $Pr \leq 0.8$. In this figure, we observe three profiles that depict the quadratic nature in the stability limits of both types of hexagons and of the primary rolls obtained by weakly non-linear analysis, [24]. These profiles indicate that there is a loss of stability for both "up" and "down" hexagons (see also Fig. 7 for contour plots of these types of hexagons, illustrating up-welling, Fig. 7a, and down-welling Fig. 7b in the center) at $Pr_c = 0.2506$, where at this point primary rolls become the stable planform. For $Pr \ll Pr_c$, "up" hexagons were found to be stable, while for $Pr \gg Pr_c$, the stable planform is that of "down" hexagons (see Appendix).

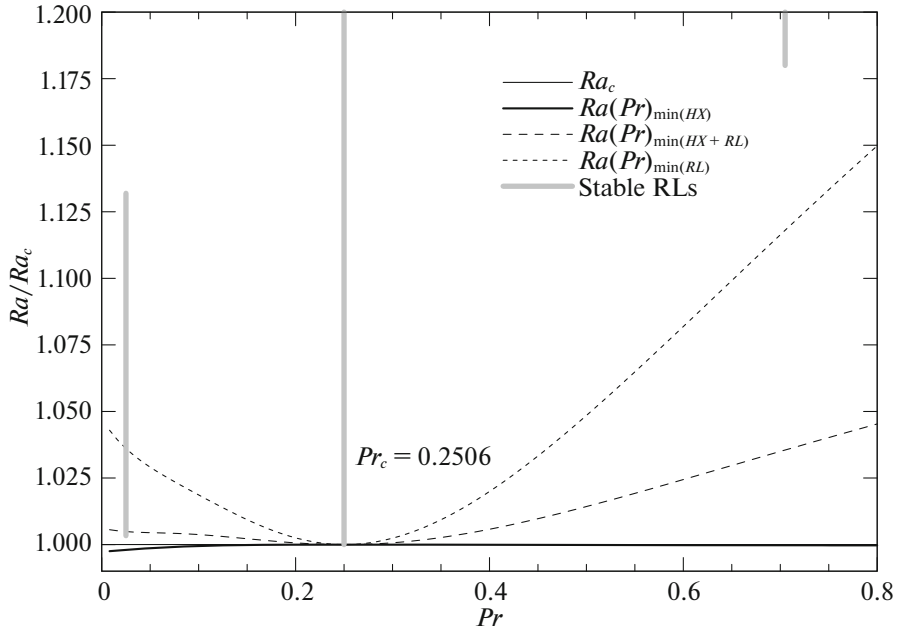

Fig. 6. The change in the stability of subcritical hexagons and rolls as a function of Prandtl number. Black curves correspond to the limits predicted by [24]. Grey curves and dotted lines summarise current calculations for the rolls.

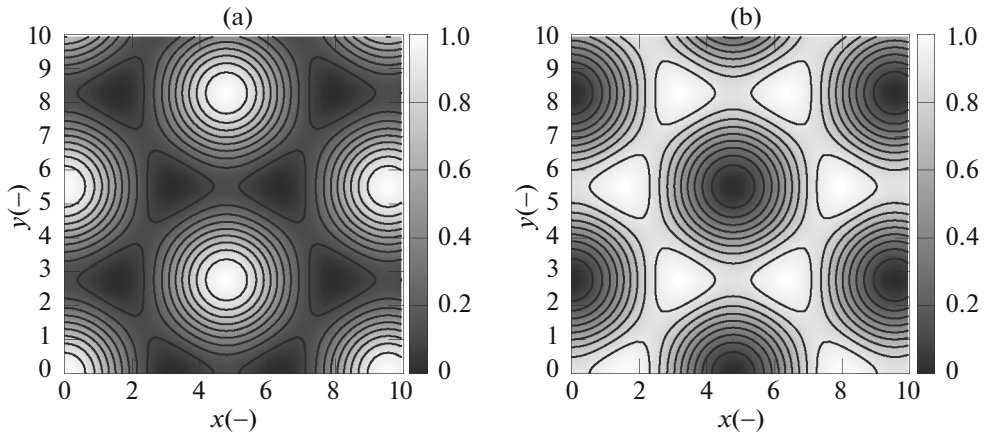

Fig. 7. Contour plots of the temperature perturbation of stable "up" ($Pr = 0.025$) and "down" ($Pr = 0.705$) hexagons at $Ra \approx 1.01 Ra_c$. Here the x and y coordinates are functions of the wavelength and the temperature is normalised by $(T - T_{\min}) \,/\, (T_{\max} - T_{\min})$.

In addition to the profiles of Ra as a function of Pr in Fig. 6 [24], we examine the stability of hexagons and rolls obtained from a fully non-linear analysis conducted here for $Pr = 0.025, 0.25, 0.705$. We summarize the data obtained for the rolls in the earlier subsections by indicating the minimum and maximum eigenvalue growth rate points of the stable region associated with the corresponding critical wavenumber. Finally, we observe in Fig. 8 the consequences of the change in stability of the different planforms on the variation of the mean convective temperature at the lower insulating boundary as heating is applied. We find, as expected, that at lower Prandtl numbers (i.e., $Pr \leq 0.25$), the hydrodynamic effects influence the change in the convective temperature. This is indicated by the hexagon states displaying a significantly lower convective temperature than the rolls at an equivalent Ra. This effect decreases with increasing Prandtl number; for example, at $Pr = 0.705$, the mean convective temperatures arising from the hexagonal states are only slightly less than those for the rolls, while at $Pr = 7.0$, the hexagonal states have a higher mean convective temperature than the rolls.

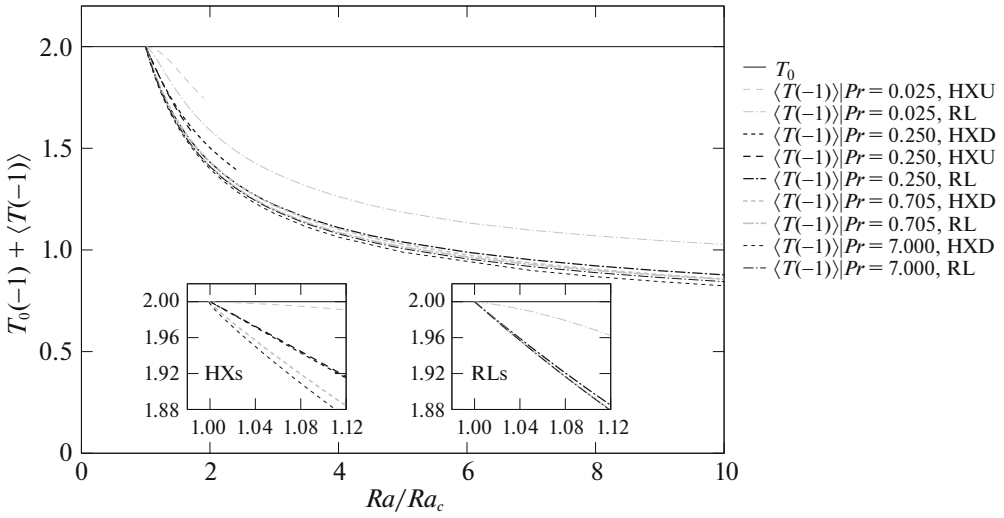

Fig. 8. Variation of mean temperature due to convection at the insulating surface ($\langle T(-1)\rangle$) with heating applied (Ra/Ra_c) for rolls and hexagons for $Pr = 0.025, 0.25, 0.705, 7.0$. Note that "up" and "down' hexagons are indicated with HXU and HXD.

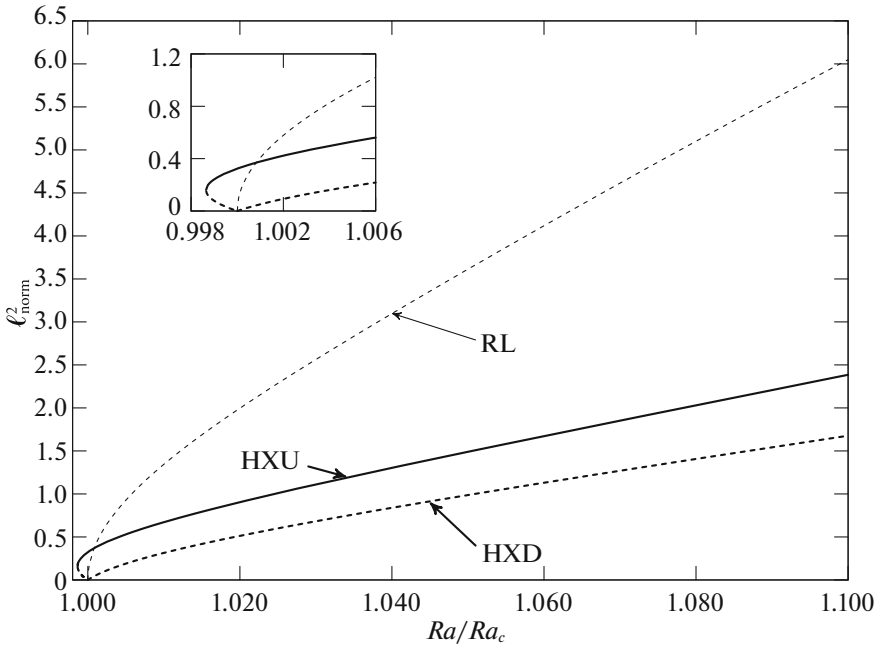

Fig. 9. Sequences of hexagonal and roll convections beyond the critical transition at $Pr = 0.025$. Amplitudes are indicated by ℓ^2_{norm}.

4. SUMMARY AND DISCUSSION

In this work, we presented a stability analysis of the flow in a horizontal layer, which is driven by uniform heating. We performed linear stability analysis and obtained neutral curves for various values of the Pr number. Non-linear results for equilibrium states were also obtained with the aid of a Newton–Raphson iterative method. We showed that the equilibrium states bifurcate both subcritically and supercritically depending on their relevant wavenumber and Prandtl number allocation.

We subsequently studied the stability of non-linear equilibrium states by employing standard linear stability theory. We superimposed the general type of three-dimensional disturbances on the equilibrium roll states. The stability ranges were found to be bounded by the E, CR, HX, K, O, SV, and ZZ instability boundaries (Table 3). Oscillating forms of the E, HX, K, SV, and ZZ instabilities were also found. It

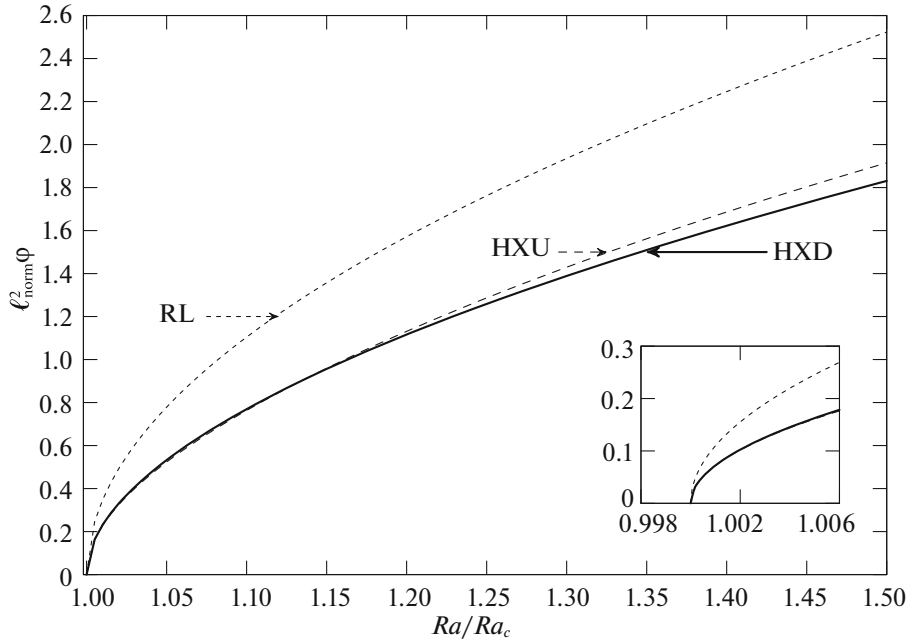

Fig. 10. Sequences of hexagonal and roll convections beyond the critical transition at $Pr = 0.250$. Amplitudes are indicated by ℓ^2_{norm}.

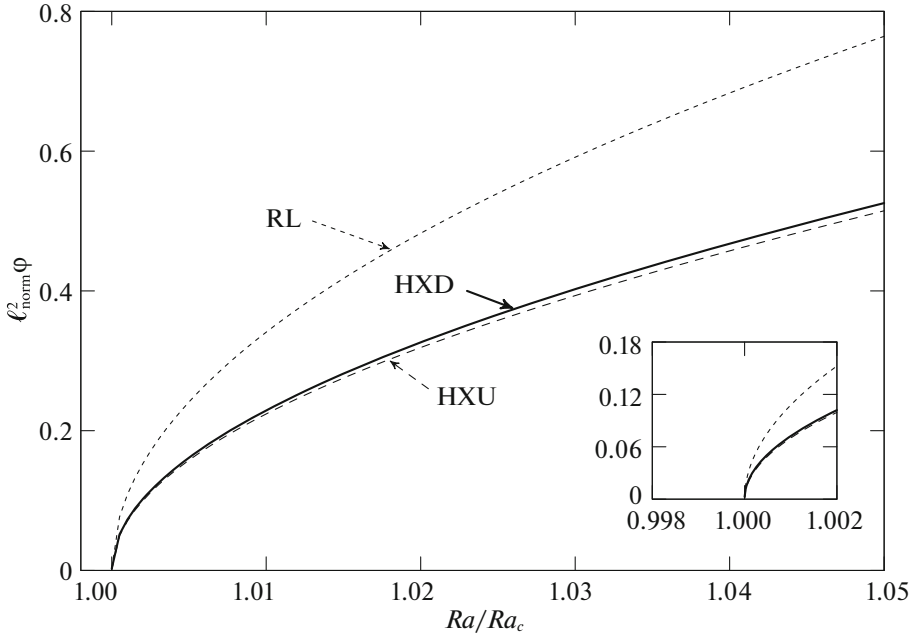

Fig. 11. Sequences of hexagonal and roll convections beyond the critical transition at $Pr = 0.255$. Amplitudes are indicated by ℓ^2_{norm}.

was confirmed as is well known, that the Eckhaus curve bounded the range of stable secondary flow towards larger and smaller wavenumbers. It was found that, in general, the values of d that determined the sideband stability region varied in the regime $0.1 \leq d \leq 0.2$ as indicated in the figures depicting the stability regions, for all Pr values that we examined. The stability boundary of the secondary flow towards larger values of Ra was established via an oscillatory/monotonic bifurcation curve, indicating that the secondary flow is either time varying (oscillatory) or stationary, depending on the nature of the

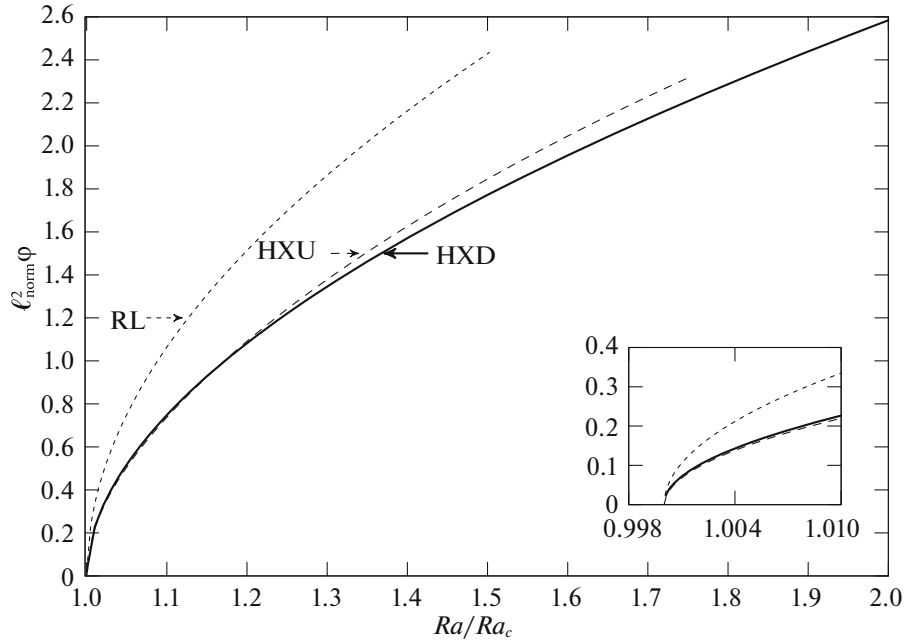

Fig. 12. Sequences of hexagonal and roll convections beyond the critical transition at $Pr = 0.260$. Amplitudes are indicated by ℓ^2_{norm}.

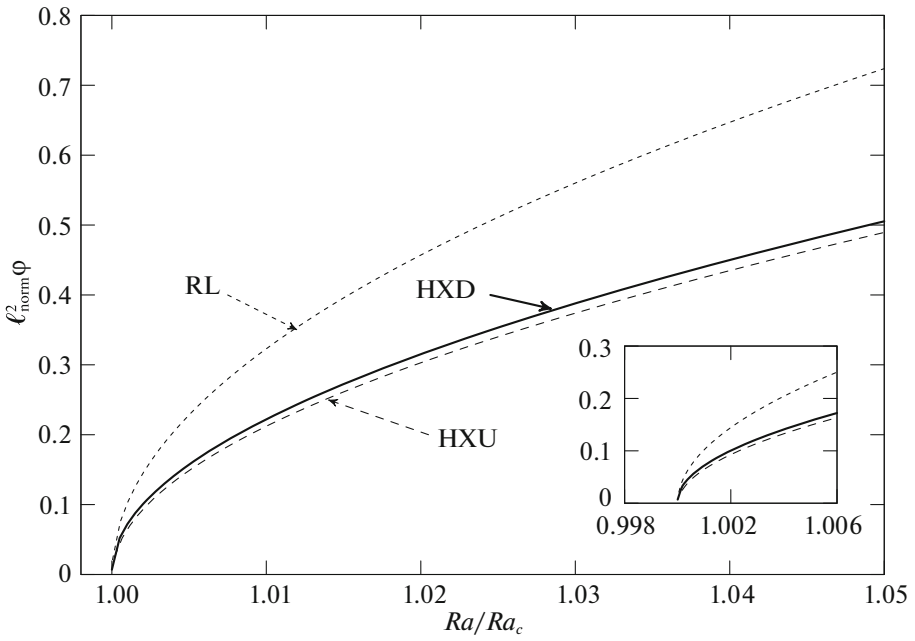

Fig. 13. Sequences of hexagonal and roll convections beyond the critical transition at $Pr = 0.270$. Amplitudes are indicated by ℓ^2_{norm}.

perturbations introduced. This indicates that for these cases of Pr, the solutions are nonlinear states that effect heat transport via oscillatory waves.

We found regions of steady rolls for $Pr = (0.025, 0.25, 0.705, 7)$ that are consistent with earlier theoretical analyses investigating roll structures in the Rayleigh Bénard problem [9, 15, 16]. It is expected that in the regions where we find that the rolls are stable for all Pr considered, there could

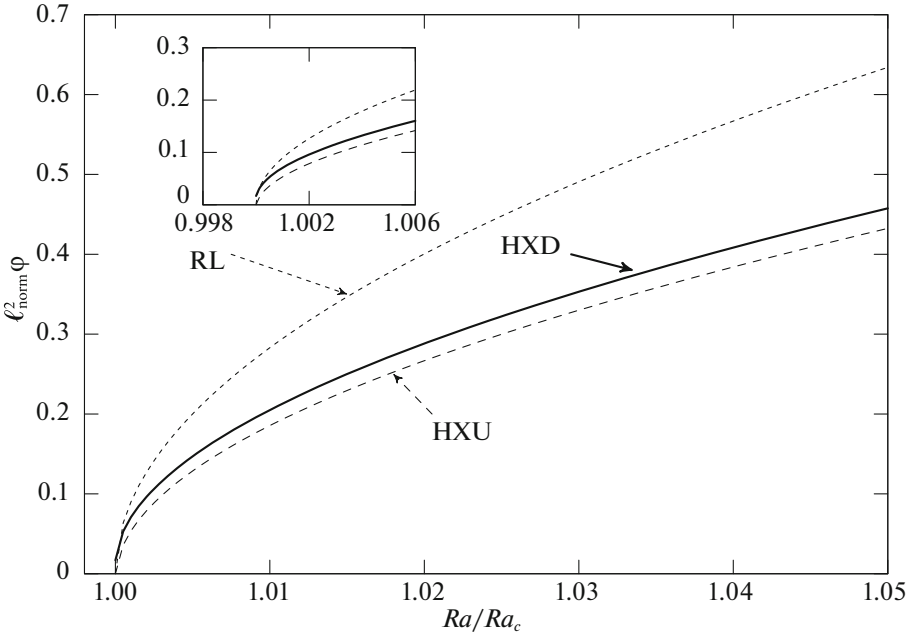

Fig. 14. Sequences of hexagonal and roll convections beyond the critical transition at $Pr = 0.310$. Amplitudes indicated by ℓ^2_{norm}.

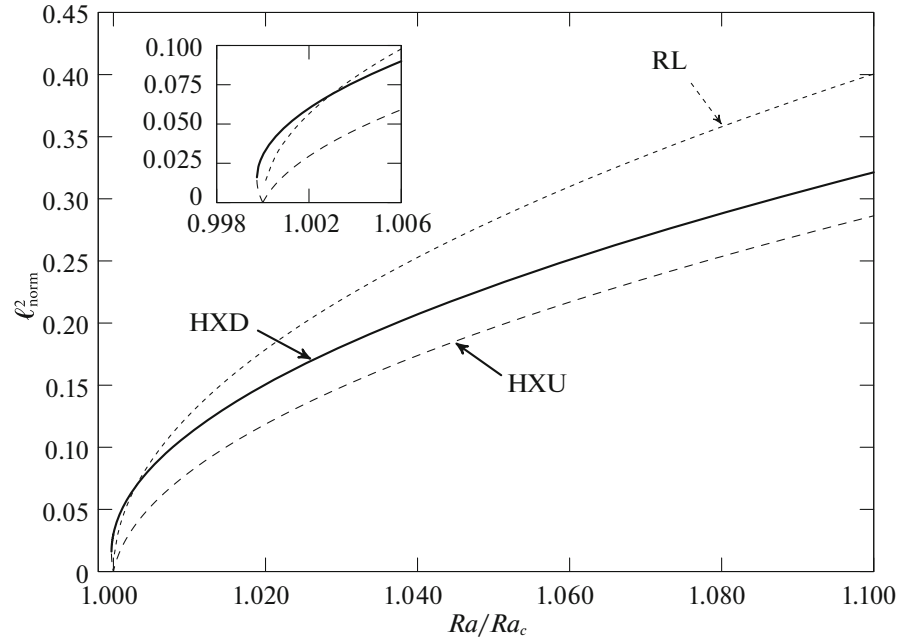

Fig. 15. Sequences of hexagonal and roll convections beyond the critical transition at $Pr = 0.705$. Amplitudes indicated by ℓ^2_{norm}.

be a bistability or competition between the roll and hexagon states [10]. Further research on the stability of the hexagons and the potential bistability with rolls is on-going. It is important to note that, as far as the authors are aware, no experimental studies have been performed that seek steady rolls in the regions in question. Carrigan [7] provided the only known study where attempts were made to find steady rolls at $Ra = 18Ra_c$, $Pr = \infty$, and $\alpha > \alpha_c$.

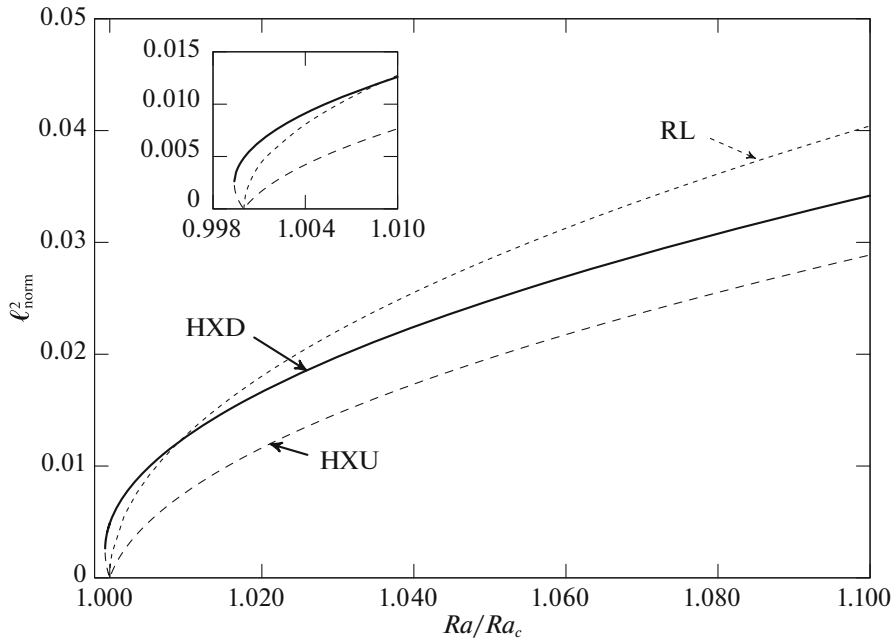

Fig. 16. Sequences of hexagonal and roll convections beyond the critical transition at $Pr = 7.000$. Amplitudes indicated by ℓ^2_{norm}.

Table 3. Properties defining the roll instabilities, for $\alpha_c = 1.315$

Instability	Abbreviation	b	d	Im(σ)
Cross-roll	CR	$>\alpha_c$	0	0
Eckhaus	E	0	$\ll\alpha_c$	0
Hexagonal	HX	$\frac{\alpha_c}{2}$	$\frac{\sqrt{3}\alpha_c}{2}$	0
		$\frac{\sqrt{3}\alpha_c}{2}$	$\frac{\alpha_c}{2}$	0
Knot	K	$<\alpha_c$	0	0
Oscillatory	O	$<\alpha_c$	0	Pair
Skewed-varicose	SV	$<\alpha_c$	$<\alpha_c$	0
Zig-zag	ZZ	$\ll\alpha_c$	0	0

APPENDIX

In this Appendix data are presented, by plotting the amplitudes for hexagonal and roll states as the conductive laminar fluid state bifurcates to convective fluid states. Figures 9–16 support Fig. 6 of the main paper. The meaning of the various curves for the hexagons and rolls is as follows: thick lines—"down" hexagons; long dashed lines—"up" hexagons; short dashed lines—rolls.

FUNDING

The work presented here was funded by a Marie-Curie Intra-European Fellowship (Contract no. 274367) of the European Commission's FP7 People Programme (GCG). We are grateful for the support of a visiting Professorship by the Leverhulme Trust, which resulted in many fruitful discussions and suggestions.

REFERENCES

1. G. M. Gershuni, E. M. Zhukhovitsky, and A. A. Yakimov, "On stability of plane-parallel convective motion due to internal heat sources," Int. J. Heat Mass Transf. **17**, 717–726 (1974).
2. M. Nagata and S. Generalis, "Transition in convective flows heated internally," J. Heat Transf. **124**, 635 (2002).
3. S. Generalis and M. Nagata, "Transition in homogeneously heated inclined plane parallel shear flows," J. Heat Trans. **125**, 795 (2003).
4. G. M. Cartland Glover and S. C. Generalis, "Pattern competition in homogeneously heated fluid layers," Eng. Appl. Comput. Fluid Mech. **3**, 164–174 (2009).
5. G. M. Cartland Glover, K. Fujimura, and S. C. Generalis, "Pattern formation in volumetrically heated fluids," Chaos Simul. Modell. Int. J. **2013**, 164 (2013).
6. G. M. Cartland Glover, K. Fujimura, and S. C. Generalis, in *Proceedings of the 15th International Topical Meeting on Nuclear Reactor Thermal-Hydraulics* (Pisa, Italy, 2013), p. 286.
7. C. R. Carrigan, "Convection in an internally heated, high Prandtl number fluid. A laboratory study," Geophys. Astrophys. Fluid Dyn. **32**, 1–21 (1985).
8. H. Bénard, "Les tourbillons cellulaires dans une nappe liquide," Rev. Gen. Sci. Pures Appl. **11**, 1271–1309 (1900).
9. F. H. Busse, "Non-linear properties of thermal convection," Rep. Prog. Phys. **41**, 1929 (1978).
10. F. H. Busse, "Remarks on the critical value $P_c = 0.25$ of the Prandtl number for internally heated convection found by Tveitereid and Palm," Eur. J. Mech. B **47**, 32–34 (2014).
11. K. E. Daniels, B. B. Plapp, and E. Bodenschatz, "Pattern formation in inclined layer convection," Phys. Rev. Lett. **84**, 5320 (2000).
12. C. Q. Hoard, C. R. Robertson, and A. Acrivos, "Experiments on the cellular structure in Bénard convection," Int. J. Heat Mass Transf. **13**, 849 (1970).
13. F. H. Busse, "The stability of finite amplitude cellular convection and its relation to an extremum principle," J. Fluid Mech. **30**, 625 (1967).
14. F. H. Busse and J. A. Whitehead, "Instabilities of convection rolls in a high Prandtl number fluid," J. Fluid Mech. **76**, 305 (1971).
15. R. M. Clever and F. H. Busse, "Large wavelength convection rolls in low Prandtl number fluids," Zs. Angew. Math. Phys. **29**, 711 (1978).
16. F. H. Busse and R. M. Clever, "Instabilities of convection rolls in a fluid of moderate Prandtl number," J. Fluid Mech. **91**, 319 (1979).
17. F. H. Busse and E. W. Bolton, "Stability of convection rolls in a layer with stress-free boundaries," J. Fluid Mech. **146**, 115 (1984).
18. R. Clever and F. H. Busse, "Transition to time-dependent convection," J. Fluid Mech. **65**, 625 (1974).
19. F. A. Kulacki and R. J. Goldstein, "Thermal convection in a horizontal fluid layer with uniform volumetric energy sources," J. Fluid Mech. **55**, 271 (1972).
20. J. Takahashi, Y. Tasaka, Y. Murai, Y. Takeda, and T. Yanagisawa, "Experimental study of cell pattern formation induced by internal heat sources in a horizontal fluid layer," Int. J. Heat Mass Transf. **53**, 1483 (2010).
21. Y. Tasaka, Y. Kudoh, Y. Takeda, and T. Yanagisawa, "Experimental investigation of natural convection induced by internal heat generation," J. Phys.: Conf. Ser. **14**, 168 (2005).
22. H. Ichikawa, K. Kurita, Y. Yamagishi, and T. Yanagisawa, "Cell pattern of thermal convection induced by internal heating," Phys. Fluids **18**, 038101 (2006).
23. D. J. Tritton and M. N. Zarraga, "Convection in horizontal layers with internal heat generation," J. Fluid Mech. **30**, 21 (1967).
24. M. Tveitereid and E. Palm, "Convection due to internal heat sources," J. Fluid Mech. **76**, 481 (1976).
25. R. Thirlby, "Convection in an internally heated layer," J. Fluid Mech. **44**, 673 (1970).
26. A. Thess and M. Bestehorn, "Planform selection in Benard-Marangoni convection: L hexagons versus G hexagons," Phys. Rev. E **52**, 6358 (1995).
27. E. W. Schwiderski and H. J. A. Schwab, "Convection experiments with electrolytically heated fluid layers," J. Fluid Mech. **48**, 707 (1971).
28. P. H. Roberts, "Convection in horizontal layers with internal heat generation," J. Fluid Mech. **30**, 33 (1967).
29. Y. Tasaka and Y. Takeda, "Effects of heat source distribution on natural convection induced by internal heating," Int. J. Heat Mass Transf. **48**, 1164 (2005).
30. V. V. Kolmychkov, O. S. Mazhorova, and O. V. Shcheritsa, "Numerical study of convection near the stability threshold in a square box with internal heat generation," Phys. Lett. A **377**, 2111 (2013).
31. Lord Rayleigh, "On convection currents in a horizontal layer of fluid, when the higher temperature is on the under side," Philos. Mag., Ser. 6 **32** (192), 529 (1916).
32. J. Boussinesq, "Sur le pouvoir refroidissant d'un courant liquide ou gazeux," J. Phys. Theor. Appl. **1**, 71 (1902).
33. S. C. Generalis and F. H. Busse, in *Proceedings of the 5th European Thermal-Sciences Conference* (Eindhoven, the Netherlands, 2008), p. FCV10.
34. T. Akinaga, S. C. Generalis, and F. H. Busse,"Tertiary and quaternary states in the Taylor-Couette system," Chaos Solitons Fractals **109**, 107 (2018).